Chapter 2
The Helium-3 Spin-Echo Experiment

Helium-3 spin-echo (HeSE) is a novel technique uniquely sensitive to adsorbate diffusion on atomic length- and pico- to nanosecond timescales [1, 2]. This chapter introduces the principles underlying the experiment and presents typical data analysis methods. First, the helium atom scattering (HAS) technique is presented, with a general description of its use for structural studies, as well as dynamics measurements using quasi-elastic helium atom scattering (QHAS). Subsequently, the spin-echo principle is described and the Cambridge spectrometer presented. The final section introduces standard data analysis techniques to set the scene for the following chapters.

2.1 Helium Atom Scattering

In a HAS experiment a thermal beam of helium atoms is scattered from a crystal surface inside an ultra high vacuum (UHV) chamber and the intensity of the scattered beam is measured by a detector [3]. The use of helium atoms makes the technique exceptionally surface sensitive as they interact with the outermost surface electrons and do not penetrate the bulk. Furthermore, the low beam energies involved (typically between 5 and 100 meV) and the inertness of helium imply that HAS is a non-destructive technique, permitting the investigation of biological samples that would degrade in a more energetic beam or when using charged probes, for example during low energy electron diffraction (LEED) experiments.

The principle of atom scattering is illustrated in Fig. 2.1. Like other scattering techniques, HAS provides experimental results in momentum transfer space [4]. The left-hand side of Fig. 2.1 defines the conventional nomenclature for the incident and outgoing wavevectors, $\boldsymbol{k}_i$ and $\boldsymbol{k}_f$. Specular reflection occurs when the incident scattering angle, Θ_i, is equal to the outgoing angle, Θ_f, and the total scattering angle of an experiment is defined as $\Theta = \Theta_i + \Theta_f$. The momentum transfer parallel to the surface, $\Delta\boldsymbol{K} = \boldsymbol{K}_f - \boldsymbol{K}_i$, can be calculated from the scattering geometry as $\Delta\boldsymbol{K} = k_i \sin\Theta_i - k_f \sin\Theta_f$. The right-hand part of Fig. 2.1 illustrates scattering from

B. A. J. Lechner, *Studying Complex Surface Dynamical Systems Using Helium-3 Spin-Echo Spectroscopy*, Springer Theses, DOI: 10.1007/978-3-319-01180-6_2,

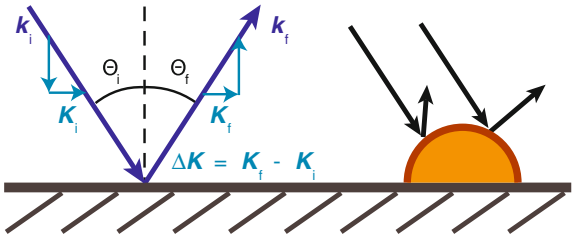

Fig. 2.1 Schematic illustration of a helium atom scattering experiment. The wavevectors are denoted as $\boldsymbol{k_i}$ for the incident and $\boldsymbol{k_f}$ for the outgoing beam. By convention, the components parallel to the surface are given in capital letters, $\boldsymbol{K_i}$ and $\boldsymbol{K_f}$, and the momentum transfer parallel to the surface is $\Delta\boldsymbol{K} = \boldsymbol{K_f} - \boldsymbol{K_i}$. The incident and outgoing scattering angles are written as Θ_i and Θ_f, respectively. The total scattering angle is $\Theta = \Theta_i + \Theta_f$. The *right-hand* side diagram illustrates scattering from an adsorbate, where the *shaded* region indicates the area around the adsorbate that the helium atoms scatter from. The scattering cross section of an adsorbate is typically much larger than its size

an isolated adsorbate particle. Due to their interaction with the outermost electrons of a surface species, helium atoms are extraordinarily sensitive to individual defects and small species such as hydrogen atoms. The apparent cross section of an adsorbate in a helium beam is typically much larger than the actual size of the atom or molecule [5].

2.1.1 Diffraction Measurements

The helium beam has a wavelength comparable with atomic spacings and therefore a diffraction pattern is generated during scattering which contains information about the surface structure [3]. Each substrate atom or adsorbate can be considered as a point scatterer in the helium beam. The kinematic scattering approximation defines the scattered amplitude as the product of a form factor, F, describing scattering from each individual scatterer, and an amplitude structure factor, S_a, which contains information about the distribution of all scatterers on the surface and is coverage-dependent [2]. The total scattered amplitude at a certain position in momentum transfer is given as

$$\Phi_{total}(\Delta\boldsymbol{K}) = \sum_j F_j(\Delta\boldsymbol{K}) \cdot \exp(-i\,\Delta\boldsymbol{K} \cdot \boldsymbol{R}_j), \tag{2.1}$$

where F_j is the form factor and $\boldsymbol{R}_j$ the position of the jth scatterer. If the form factor for all scatterers is the same, i.e. all scattering centres are identical, the equation can be simplified to

$$\Phi_{total}(\Delta\boldsymbol{K}) = F(\Delta\boldsymbol{K}) \cdot \sum_j \exp(-i\,\Delta\boldsymbol{K} \cdot \boldsymbol{R}_j) = F(\Delta\boldsymbol{K}) \cdot S_a(\Delta\boldsymbol{K}). \tag{2.2}$$

The scattered intensity is obtained from $I = |F(\Delta \boldsymbol{K})|^2 \cdot |S_a(\Delta \boldsymbol{K})|^2$. Helium atoms have a de Broglie wavelength on the order of Ångströms, ensuring resolution of atomic scale features during a HAS experiment.

Helium atom scattering instruments can be divided into two main types, "fixed angle" machines, where the angle between incident and outgoing beam is fixed, and movable systems, where a rotating detector alters the total scattering angle, Θ [5]. All experiments presented in this thesis are from fixed angle instruments, the Cambridge HeSE spectrometer (cf. Sect. 2.3) and a separate atom scattering apparatus which is presented in Chap. 3. In a fixed angle scattering experiment, the incident and outgoing scattering angles are determined by the orientation of the crystal which can be rotated around the vertical centre axis of the scattering chamber. In contrast to diffraction experiments with rotating detector arms, where the incident scattering angle can be kept constant, turning the sample in a fixed angle machine always alters the incident and outgoing scattering angles at the same time. Diffraction measurements performed in a fixed angle scattering apparatus are therefore intrinsically asymmetric, even for a perfectly aligned crystal. The heights of equivalent diffraction peaks either side of specular are therefore different, which needs to be considered in data analysis and when comparing diffraction scans with results from different instruments or simulations.

2.1.2 Adsorption and Desorption Studies

In addition to diffraction experiments, measurements of the specular helium reflectivity can provide information about the degree of order on the surface [5]. The intensity of the specular beam is greater for a highly ordered surface as less signal is lost in other scattering directions. Measuring the proportion of incident helium that is scattered into the specular beam is a means of determining the quality of a substrate surface as it is reduced by step edges and defects. Equally, monitoring the specular helium reflectivity during a dosing or desorption process can provide information about the change in order on the surface.

A dosing process can be monitored by recording the specular helium reflectivity as a function of exposure. The resulting curve is generally termed an "uptake" curve. Adsorption onto a clean and flat substrate initially reduces the degree of order on the surface, resulting in lower reflectivity towards the helium beam. When regular structures are formed, the degree of order and thus the helium reflectivity increase. Uptake curves are useful for estimating the coverage at a given specular attenuation level, to study the lateral interactions between adsorbates and to determine where regular overlayer structures occur [5]. In the low coverage limit, the total scattering cross section, Σ, for isolated adsorbates can be calculated as

$$\Sigma = -\frac{1}{n_s} \cdot \frac{1}{I_0} \cdot \left. \frac{dI}{d\Theta} \right|_{\Theta=0}, \tag{2.3}$$

where Θ is the coverage given by the number of adsorbates per substrate atom, n_s is the number of substrate atoms per unit area, and I/I_0 is the specular helium beam attenuation at coverage Θ. If one can assume non-interacting adsorbates occupying random adsorption sites with large cross sections that overlap, then the formula also holds at higher coverages,

$$\Sigma = -\frac{1}{n_s} \cdot \frac{1}{I_0} \cdot \frac{dI}{d\Theta}, \tag{2.4}$$

hence

$$\frac{I}{I_0} = \exp\left(-\Theta \Sigma n_s\right). \tag{2.5}$$

Equation 2.5 implies that the specular attenuation as a function of coverage is linear on a logarithmic scale, in the simplest case. The scattering cross sections of repelling adsorbate particles overlap less, increasing the total cross section seen by the helium beam compared to that for non-interacting adsorbates and thus the uptake curve falls below the linear line. When attractive interactions influence the distribution of adsorbate particles, on the other hand, the curve rises above linear.

In a similar way, a desorption process can be monitored with specular helium reflectivity. In the case of molecular desorption, reversal of the uptake curve is observed, while disordering or decomposition of adsorbates typically results in a drop in the observed reflectivity.

2.1.3 Measuring Surface Dynamics

In addition to structural studies, HAS can be used to investigate surface dynamics by measuring the difference in energy distribution in the beam before and after scattering from the sample [3, 6]. The technique is termed quasi-elastic helium atom scattering (QHAS).

In a QHAS experiment, the energy spectrum of the scattered helium beam is determined [3, 6]. If the surface remains static during the scattering event, the helium atoms are scattered elastically, resulting in a peak in the energy domain with a finite width determined by the velocity spread in the beam and properties of each individual instrument. In case of non-periodically moving adsorbates, however, the elastic peak is broadened by a quantum mechanical form of Doppler broadening—hence the name "quasi-elastic". In addition, the helium beam can excite or de-excite surface phonons, resulting in an inelastic peak in the energy spectrum, where the energy difference between elastic and inelastic peak is defined by the energy loss or gain during the scattering process [7]. A QHAS experiment is the surface sensitive analogue of quasi-elastic neutron scattering which measures diffusion in bulk materials [8]. Therefore, the existing theoretical framework for the neutron scattering experiments could be adopted for the QHAS technique.

Theoretical foundations are in Van Hove's scattering theory describing motion by the Van Hove pair correlation function $G(\boldsymbol{R}, t)$ which defines the probability of

finding an atom at position $\boldsymbol{R}$ at the time t given the presence of an atom (the identical or a different one) at the origin at $t = 0$ [9]. It is possible to divide $G(\boldsymbol{R}, t)$ into

$$G(\boldsymbol{R}, t) = G_S(\boldsymbol{R}, t) + G_D(\boldsymbol{R}, t), \tag{2.6}$$

where $G_S(\boldsymbol{R}, t)$ is the self-correlation function, describing the probability of finding the same atom at $\boldsymbol{R}$ and t given it was at the origin at $t = 0$, and $G_D(\boldsymbol{R}, t)$ the distinct correlation function, relating the position of two distinct atoms. Vineyard showed that $G_D(\boldsymbol{R}, t)$ can be written in terms of $G_S(\boldsymbol{R}, t)$ for non-interacting particles—which is typically true in the low coverage limit—and the Van Hove correlation function can be expressed in terms of the self-correlation function alone [10], facilitating the interpretation of experiments.

Within the kinematic scattering approximation, the probability of scattering into a given angle, $\partial\Omega$, and energy, $\partial\omega$, is related to the pair correlation function through

$$\begin{aligned}\frac{\partial^2 \boldsymbol{R}}{\partial\Omega\partial\omega}(\Delta\boldsymbol{K}, \omega) &= n_d |F(\Delta\boldsymbol{K}, \omega)|^2 \int\int G(\boldsymbol{R}, t) \exp[i(\Delta\boldsymbol{K}\boldsymbol{R} - \omega t)] d\boldsymbol{R} dt \\ &= n_d |F(\Delta\boldsymbol{K}, \omega)|^2 S(\Delta\boldsymbol{K}, \omega),\end{aligned} \tag{2.7}$$

where n_d is the density of adsorbates on the surface [9]. The dynamical structure factor (DSF), $S(\Delta\boldsymbol{K}, \omega)$, is an intensity structure factor and is the Fourier transform of the correlation function in space and time. The Fourier transform of the correlation function in space is called the intermediate scattering function (ISF) $I(\Delta\boldsymbol{K}, t)$, which is related to the DSF by a temporal Fourier transform:

$$G(\boldsymbol{R}, t) \overset{FT}{\Longleftrightarrow} I(\Delta\boldsymbol{K}, t) \overset{FT}{\Longleftrightarrow} S(\Delta\boldsymbol{K}, \omega). \tag{2.8}$$

The original QHAS experiments were carried out with a time-of-flight (TOF) detection system, where a chopped beam is scattered from the surface and its velocity after the scattering event is measured [11]. Any changes in velocity can be related to dynamical processes on the surface during the scattering process. TOF experiments provide a measure of the DSF, giving an inelastic peak for phonon excitations and an energy broadening, ΔE, of the elastic peak for scattering from aperiodically diffusing adsorbates. Measurements of the dependence of ΔE on the momentum transfer parallel to the surface, $\Delta\boldsymbol{K}$, provide information about the diffusion process.

The main limitation of the QHAS-TOF technique is its requirement for high energy resolution so that the broadening of the elastic peak can be determined. The elastic energy peak is convoluted with experimental factors such as the energy distribution in the incident helium beam and the chopper time resolution, limiting the energy resolution to approximately 0.3 meV [3]. Therefore, the time-of-flight technique can only be applied to exceptionally fast moving systems, putting it at the lower end of the timescale in Fig. 1.1. HeSE, on the other hand, provides a direct measure of the energy broadening, allowing for the investigation of diffusion on pico- to nanosecond timescales, as explained in the following section.

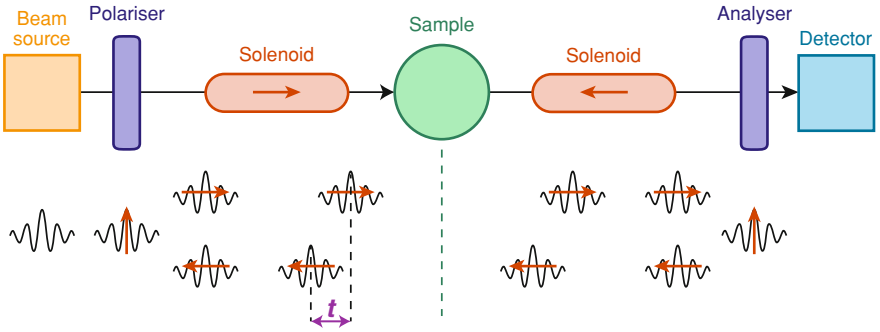

Fig. 2.2 Schematic overview of the helium-3 spin-echo experiment. The different components of the instrument are outlined in the *top row*, while the spin state of the wavepackets of the helium-3 beam during the experiment is illustrated below. The first solenoid field splits the helium-3 atom into two wavepackets which reach the sample separated by a time, t. A second solenoid recombines the two components. If the two wavepackets do not recombine to give the same final spin state, a reduction in polarisation is measured in the detector

2.2 Helium-3 Spin-Echo Spectroscopy

While QHAS-TOF operates in the energy domain, HeSE instead investigates the time domain, providing a measure of the ISF. Experimental results are therefore the temporal Fourier transform of TOF measurements. The key advantage of the HeSE technique is that it measures the energy change directly, rather than in relation to the energy of the helium beam, thus increasing the resolution of the experiment by two orders of magnitude over QHAS-TOF [3]. Measurements are typically analysed directly in the time domain to study aperiodic diffusion, or can be Fourier transformed into an energy spectrum for the investigation of periodic motion such as phonons.

The principle underlying helium-3 spin-echo is to use the nuclear spin of a helium-3 atom as an internal timer [2, 4, 12, 13], in analogy to the neutron spin-echo technique [14], all the while retaining the non-destructive nature and surface sensitivity of the HAS experiment. See Fig. 2.2 for an illustration of the setup of a HeSE experiment. A supersonic helium beam source creates a beam of helium-3 atoms which is then polarised in a direction perpendicular to the beam axis by the combination of a hexapole magnet focussing one spin polarisation (defocussing the other) and a dipole magnet that aligns all the spins in the same direction. A variable magnetic field parallel to the beam direction is created in a solenoid, splitting the helium wavepacket into two spin states, parallel and antiparallel to the field. The field separates the components in both space and time. The component parallel to the field is accelerated as it enters the solenoid and the antiparallel one is decelerated, so that they reach the sample a time period, t, apart, which is called the spin-echo time. t depends on the mass of helium-3, m, its gyromagnetic ratio, γ, the mean velocity of the beam, v_0, and the magnetic field integral along the path of the beam [2]:

$$t = \frac{\hbar\gamma}{m v_0^3} \int B dl. \tag{2.9}$$

After scattering from the sample surface the two components are recombined in an identical but reversed magnetic field. The scattered beam is then spin-analysed by another combination of dipole and hexapole magnets to provide a polarisation measurement as it enters the detector. If the surface remains static during the scattering process the helium atoms scatter elastically, the two spin components are recombined and the entire scattered beam passes through the analyser into the detector. If, however, the atoms or molecules on the surface move during t, the two components do not scatter identically and therefore do not recombine to give the same final spin-state, resulting in a reduction in net polarisation reaching the detector. HeSE thus measures the coherence of the two spin components after scattering from the surface, which typically decays with time.

2.3 The Cambridge Helium-3 Spin-Echo Spectrometer

After a prototype was presented by De Kieviet and coworkers [12, 13], the Surface Physics group at Cambridge developed the first HeSE apparatus with sufficient momentum transfer space resolution to map out adsorbate diffusion, where accessible timescales range from 0.01 to 680 ps [1, 15]. Figure 2.3 shows a photograph of the apparatus, with annotations illustrating the location of the main components, in analogy to the diagram in Fig. 2.2.

The instrument is of the fixed angle type, with a total scattering angle of 44.4°, an angular resolution of 0.1° and an energy resolution of 3 μeV (or an ultimate resolution of 20 neV, corresponding to a 1 % decay in polarisation at the maximum spin-echo time) [15]. The helium beam is created in a supersonic helium beam source, which is described in detail in Chap. 4. A recycling system filters and compresses the helium-3 gas which is then expanded into the source chamber through a cooled nozzle and recirculated back into the system after expansion [15–17]. The nominal beam energy for the spectrometer is 8 meV, for which energy the magnets provide optimal focussing. Two combinations of permanent hexapole/dipole magnets spin-polarise and spin-analyse the helium-3 beam [15, 18], while a variable magnetic field in two solenoids splits and recombines the wavepackets. The magnetic field can be controlled by the current running through the two solenoids and defines the spin-echo time, t. A pair of coils mounted on the sample manipulator rotates the plane of spin polarisation when the helium atoms change direction during the scattering process.

The sample is located in the scattering chamber, mounted on a six-axis manipulator. Horizontal x/y-motion and vertical z-motion allows positioning of the sample in the location where the ingoing and outgoing beam arms meet, while rotation around the vertical centre axis (γ-rotation) changes the scattering angles, Θ_i and Θ_f. Tilting of the crystal with respect to the plane of the incident and

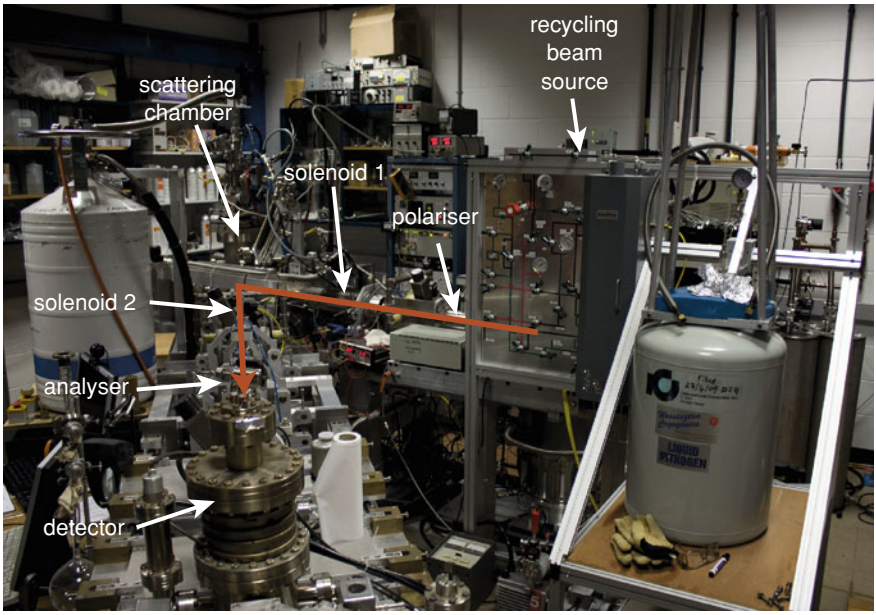

Fig. 2.3 Photograph of the Cambridge HeSE spectrometer. Annotations highlight its main components, while a *red arrow* illustrates the path of the helium beam during an experiment

outgoing beam enables alignment of the sample perpendicular to the scattering plane (β-rotation). The sixth degree of freedom is rotation within the crystal plane to change the azimuthal direction (α-rotation). A new sample transfer manipulator was recently developed, enabling the exchange of samples without breaking the vacuum, thereby maintaining UHV conditions in the chamber [19]. Sample cooling is provided through a coldfinger which can be filled with liquid nitrogen or liquid helium through a transfer tube. Temperature control is achieved using a Eurotherm controller reading the measurements from a chromel/alumel type K thermocouple connected to the sample mount and controlling the temperature by counter-heating the cooled sample radiatively using a tungsten filament. The scattering chamber is equipped with a sputter gun for cleaning the sample by ion bombardment as well as facilities for dosing gaseous, liquid and solid substances, and a mass spectrometer for the identification of components in the background gas or dosed species.

Detection of the helium beam is achieved in a custom-built helium detector [15, 20]. The helium atoms are ionised by electrons from a hot tungsten filament and pass through ion extraction optics and a magnetic sector mass filter to select mass-3 ions before they are counted in an electron multiplier. After completion of the experiments presented in this thesis, a new detector was installed on the HeSE spectrometer which uses a solenoid magnetic field to confine electrons in the ionisation region [21, 22]. The sensitivity of the new detector is improved by approximately three orders of magnitude over that of the previous HeSE detector, thus opening a completely new range of measurements.

The observable quantity in a HeSE experiment is the intensity, I, of the helium signal in the detector, which can be related to the polarisation, P, through

$$P = \frac{I_{max} - I_{min}}{I_{max} + I_{min}}. \tag{2.10}$$

The polarisation, in turn, is directly proportional to the intermediate scattering function [2]. In order to obtain maximum signal intensity in the detector, the polarisation selected by the analyser hexapole magnet must be identical to the polarisation of the beam created in the polarising hexapole. The HeSE technique thus relies on the precise measurement of the spin polarisation of the helium-3 beam. Loss of polarisation can occur through a large velocity spread in the beam, so that beam energies other than the optimal 8 meV target are present, or stray magnetic fields. To minimise stray fields, components close to the path of the helium beam are made from non-magnetic materials as well as magnetically shielded. Despite all these efforts, however, the polarisation of the beam changes over time to a certain extent, adding errors to the measurement.

During a HeSE experiment, both the real and the imaginary components of the polarisation of the beam are measured, thus allowing Fourier transformation of the spectra without imposing artificial symmetry [23]. A phase coil creates a magnetic field which switches between the two components by adding an extra $\pi/2$ to the incoming phase, thus rendering the two solenoid fields unequal. The phase coil can be used to correct for errors caused by stray fields by regular calibration to determine the currents required for obtaining either the real or the imaginary polarisation. Calibration is achieved at a position where the imaginary polarisation is known to be zero, such as at specular reflection.

Originally, a two-point measurement technique was used for HeSE experiments, measuring the real and imaginary polarisation for each point in the ISF by setting the phase coil current to the values determined during calibration. The drawback of this method is that it relies heavily on the calibration of the phase coil current, as illustrated in Fig. 2.4, since any drifts in the polarisation are not accounted for. When looking at the two oscillating curves in the Figure, which are slightly offset from each other, it becomes apparent that the real component is not heavily dependent on ultra-precise calibration since the curve is fairly flat at this position and small errors in phase coil current thus do not change the signal intensity measured in the detector significantly. The imaginary component, however, is located on the steepest slope of the curve and even a small change in location of the exact measurement point results in a large change in intensity. To avoid such errors, a new measurement technique was recently developed [24]. Instead of attempting to measure the precise real and imaginary components, four points are measured which describe the central oscillation of the polarisation. The location of the real and imaginary component can then be determined for each individual measurement, lessening the importance of correct calibration. Furthermore, the four-point method allows the direct measurement of the polarisation rather than the intensity of the helium signal in the detector, eliminating errors due to detector and background drifts.

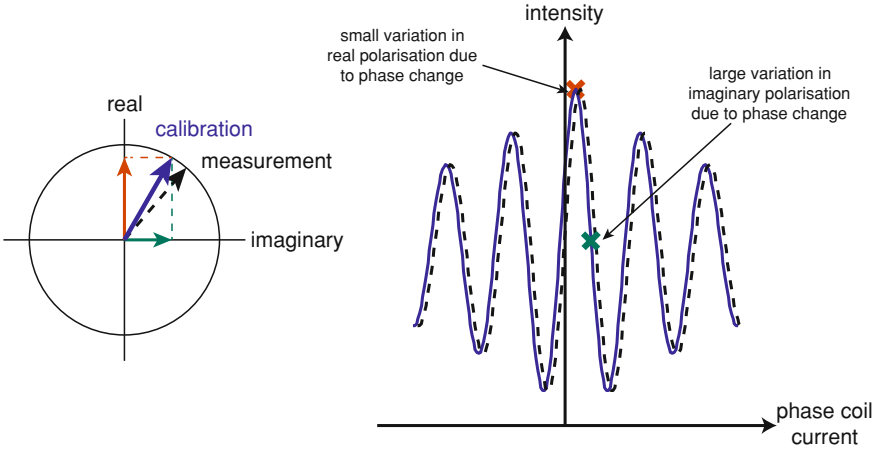

Fig. 2.4 Schematic illustration of the real and imaginary polarisation measured in a HeSE experiment. By altering the current in the phase coil and thereby the magnetic field, the polarisation of the beam is changed periodically, as illustrated by a unit circle on the *left*, and the signal intensity measured in the detector varies sinusoidally, as shown on the *right*, dependent on the proportion of the beam allowed to pass through the analyser hexapole. The phase coil is calibrated by measuring the oscillation (*solid blue line*) at a point where the imaginary polarisation is known to be zero and recording the phase coil current giving the real (*red*) and imaginary (*green*) signal, which is then used to measure the real and imaginary polarisation during a dynamics measurement. If the polarisation changes in between the calibration and the dynamics measurement, as illustrated by the *dashed line*, the measured polarisation is wrong. The error in the real component is small as the curve is relatively flat at that point while the imaginary signal exhibits large variation

For all but the very fastest diffusive motion, the real part of the polarisation is significantly larger than the imaginary one [25, 26]. Figure 2.5 shows a typical HeSE measurement of the real polarisation as a function of t, plotted as circles, and the imaginary polarisation, presented as dots. The real signal shows a large change in intensity across all timescales, while the imaginary component only exhibits an oscillatory feature at short times and drops to zero at times longer than 2 ps, which is where the diffusive motion dominates. The imaginary polarisation can thus be neglected when adsorbate diffusion is studied, as is the case for the experiments presented in this thesis. In this regime, the two- and four-point techniques show good agreement and both provide reproducible data. For measurements of phonons or other features on short timescales, however, the imaginary signal is of great importance and the four-point method is therefore much superior [24, 27].

The data presented in Chaps. 5 and 6 of this thesis were recorded using the two-point method, while the data in Chap. 7 are from four-point measurements. This is reflected in the nomenclature used in figures showing HeSE measurements where "intensity" is used for two-point, and "polarisation" for four-point measurements. Since the main focus of the thesis is the analysis of inter-cell diffusion, using only the real polarisation, both methods are equally valid. Care must be taken, however,

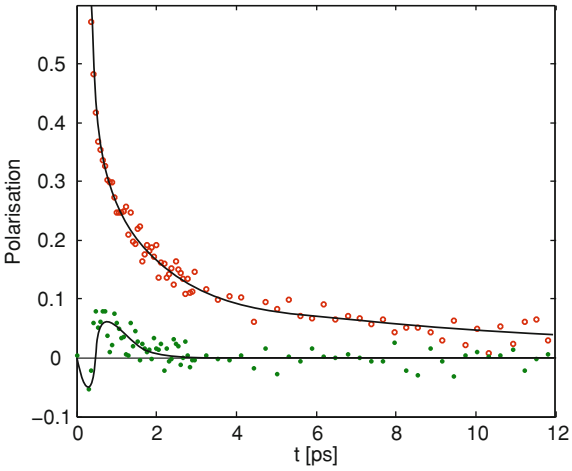

Fig. 2.5 A typical HeSE measurement, showing the real (*circles*) and imaginary polarisation (*dots*). While the real component shows a large change in signal, the imaginary contribution exhibits an oscillatory feature at very short timescales (<2 ps) but is essentially zero at larger times, where diffusive motion dominates the signal

when features on faster timescales—not discussed here—are observed as they might be influenced by inaccuracies in the calibration.

2.4 Interpreting Helium-3 Spin-Echo Data

Since HeSE measures in momentum transfer space, data interpretation is not straightforward. A typical measurement of the intermediate scattering function is shown in Fig. 2.6. On the linear time axis (left-hand side panel), details on short timescales are difficult to make out. For this reason HeSE measurements are often presented on a logarithmic scale, as illustrated in the right-hand side panel of the same figure. The two main features in this curve are oscillations at short times, t, and a global decay. Oscillations are caused by periodic motion on the surface, such as substrate phonons. To analyse such vibrational features, the spectra can be reconstructed to give the corresponding dynamical structure factor, which shows energy gain and loss peaks. The global decay, on the other hand, is a signature for aperiodic motion on the surface, such as diffusive motion of an adsorbate. To study the diffusion in more detail, the rate at which the signal decays ("dephasing rate"), α, can be determined by fitting a function of the form $f(t) = a \cdot \exp(-\alpha t) + c$, where a is the preexponential factor and c the static component. Fitting is performed using the least-squares algorithm, as implemented in Matlab. This method iteratively changes variables a, c and α to minimise the least-squares error between the measured data and the exponential function. All lines are checked by eye, to prevent misfits and to confirm that the line goes through the centre of the vibrations. α is proportional to the energy broadening of the elastic peak, ΔE, measured in QHAS-TOF experiments. The position to which the decay levels off to is called "static component" as it is typically due to

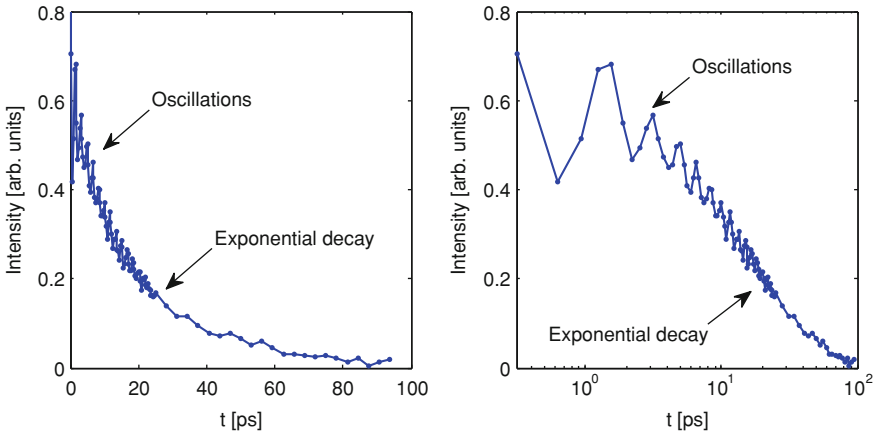

Fig. 2.6 Illustration of a typical HeSE measurement exhibiting oscillatory features and a global decay. The same data are presented on a linear (*left*) and on a logarithmic (*right*) time axis to illustrate the advantage of a logarithmic presentation, allowing simultaneous investigation of features on a range of different timescales

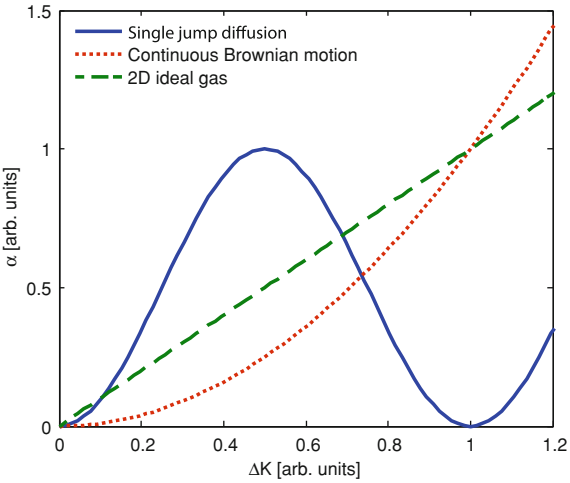

Fig. 2.7 Different types of diffusion give a different dependence of the dephasing rate on the momentum transfer. The *dotted line* shows continuous Brownian motion, which exhibits a quadratic $\alpha(\Delta \boldsymbol{K})$ dependence. Ideal gas-like diffusion shows a linear relationship (*dashed line*), while discrete hops between preferred adsorption sites give a periodic variation with $\Delta \boldsymbol{K}$, as illustrated by the *solid line*

scattering from static defects on the surface. The intensity of the static component is a diffraction pattern and thus varies with momentum transfer.

At coverages below a monolayer, many adsorbates diffuse on the substrate [28, 29]. To study this two-dimensional diffusion, HeSE measurements are performed for a range of scattering angles and along (usually two) different high symmetry crystal directions. The variation of the dephasing rate with momentum transfer parallel to the surface, $\alpha(\Delta \boldsymbol{K})$, is dependent on the exact type of diffusion. Figure 2.7 illustrates the $\alpha(\Delta \boldsymbol{K})$ dependence for three different diffusion models [3].

Continuous Brownian motion gives exponentially decaying lineshapes in the ISF and a quadratic variation of the dephasing rate with $\Delta\boldsymbol{K}$, where the proportionality factor between α and $\Delta\boldsymbol{K}^2$ is the diffusion coefficient, D:

$$\alpha = D\Delta\boldsymbol{K}^2. \tag{2.11}$$

Ideal gas-like diffusion, on the other hand, results in Gaussian lineshapes and a linear $\alpha(\Delta\boldsymbol{K})$ dependence,

$$\alpha = \sqrt{\frac{2\ln(2)k_B T}{m}}\Delta\boldsymbol{K}, \tag{2.12}$$

where the slope depends on the mass, m, of the diffusing adsorbate and the temperature, T, and k_B is the Boltzmann constant.

The most common form of diffusion is in jumps between preferred adsorption sites, on a corrugated potential energy landscape [3, 29]. In this case, the ISFs are typically of an exponentially decaying form and the $\alpha(\Delta\boldsymbol{K})$ dependence is a sum of sinusoids. The precise lineshapes and the variation of α with momentum transfer depend on the periodicity of the substrate lattice and the arrangement of the sites the adsorbate hops on, as described in the next section.

2.4.1 Jump Diffusion

The simplest form of jump diffusion occurs between sites forming a Bravais lattice, implying that the symmetry of the sites which the adsorbate occupies before and after the hop is the same. The Chudley and Elliot model for hopping motion describes the ISF as

$$I(\Delta\boldsymbol{K}, t) = \exp(-\alpha(\Delta\boldsymbol{K})\cdot t), \tag{2.13}$$

with the decay rate, α, given by

$$\alpha(\Delta\boldsymbol{K}) = 2\sum_k \nu_k \sin^2\left(\frac{\Delta\boldsymbol{K}\cdot\boldsymbol{l}_k}{2}\right), \tag{2.14}$$

where ν_k is the jump frequency, which is the inverse of the residence time, τ_k, in the adsorption site [30]. The jump vector $\boldsymbol{l}_k$ defines the direction and length of each possible hop, which depends on the substrate lattice constant.

The experiments presented in the present thesis show jump diffusion on a Cu(111) surface, schematically illustrated in Fig. 2.8. Geometrically, three types of high-symmetry sites can be distinguished: top (T), threefold hollow (H) and twofold bridge (B) sites. Copper forms a face-centred cubic (fcc) crystal structure, implying that there are two different kinds of hollow sites on the (111) surface—an hcp site on top of an atom in the second layer, and an fcc site with no atom directly underneath—which can thus be energetically different in the interaction with an adsorbate.

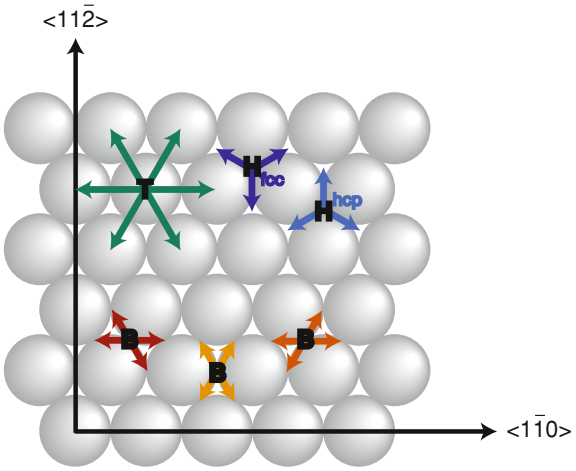

Fig. 2.8 Schematic representation of the Cu(111) surface. The possible jump vectors for single jump diffusion between equivalent sites are shown in *green* for top sites, *blue* for hollow sites and *red* for bridge sites. Furthermore, the two main high symmetry azimuthal directions are defined

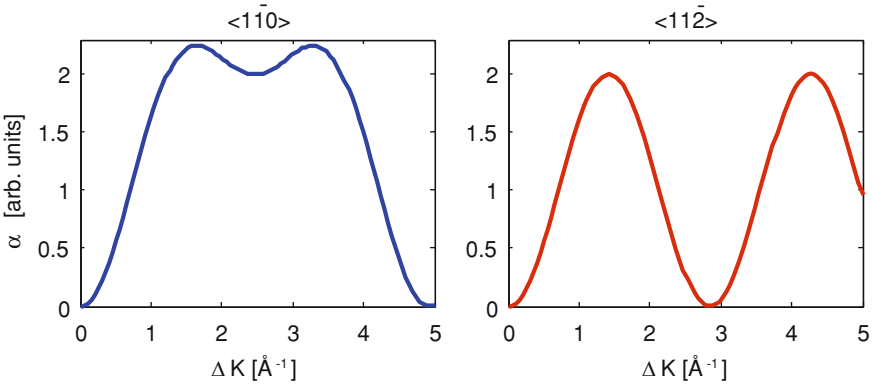

Fig. 2.9 $\alpha(\Delta \boldsymbol{K})$ dependence for hopping on a Bravais lattice of top sites (or equivalently one kind of hollow sites) on Cu(111). The projection of the jumps along the two crystal directions, $\langle 1\bar{1}0 \rangle$ and $\langle 11\bar{2} \rangle$, is different, as reflected in the periodicity of the *blue* and *red* curves

Top sites form a simple Bravais lattice on Cu(111), as well as each type of hollow site on its own, so that the Chudley and Elliot model can be used to describe the hopping motion. The $\alpha(\Delta \boldsymbol{K})$ curves predicted by the analytical model for single jumps on such a Bravais lattice projected onto the $\langle 1\bar{1}0 \rangle$ and $\langle 11\bar{2} \rangle$ azimuths are presented in Fig. 2.9, showing a simple sinusoidal form along $\langle 11\bar{2} \rangle$ and a sum of two sinusoids along $\langle 1\bar{1}0 \rangle$. Bridge sites, or both types of hollow sites together, however, form non-Bravais lattices. An adsorbate hopping on such a lattice changes the possible jump directions after each jump. In order to predict the lineshapes and

the $\alpha(\Delta \boldsymbol{K})$ dependence for hopping on such lattices, an extended model is required. Models for three-dimensional jump diffusion on non-Bravais lattices can be found in the neutron scattering literature [8, 31, 32]. These models have been adapted for QHAS experiments [33], as summarised below.

In the non-Bravais jump diffusion model, the ISF is derived from a matrix, $\boldsymbol{A}$, describing all possible jump vectors. A non-Bravais lattice consists of m different Bravais sub-lattices. Each jump is defined by a vector, $\boldsymbol{l}_{ijk}$, connecting the ith and jth sub-lattices and has a jump frequency, ν_{ijk}, which is the inverse of the residence time of the adsorbate in each site, τ_{ijk}. The total jump rate from an i site to any adjacent j site is given by a sum over all n_{ij} possible jumps,

$$\nu_{ij} = \sum_{k=1}^{n_{ij}} \nu_{ijk}. \tag{2.15}$$

The elements of matrix $\boldsymbol{A}$, which is an $(m \times m)$ matrix, are given by

$$A_{ij} = \sum_{k} \nu_{jik} \exp\left(-i \Delta \boldsymbol{K} \cdot \boldsymbol{l}_{ijk}\right) - \delta_{ij} \sum_{j'} \nu_{ij'}, \tag{2.16}$$

with k iterating over the different possible jump vectors. $\boldsymbol{A}$ can be transformed into a Hermitian matrix via

$$B = \boldsymbol{T}\boldsymbol{A}\boldsymbol{T}^{-1}, \tag{2.17}$$

where $\boldsymbol{T}$ is the similarity transformation,

$$\boldsymbol{T}_{ij} = \sqrt{\frac{1}{c_i}} \delta_{ij}. \tag{2.18}$$

As described in [33], the intermediate scattering function can then be calculated as

$$I(\Delta \boldsymbol{K}, t) = \sum_{p} w_p(\Delta \boldsymbol{K}) \exp(\alpha(\Delta \boldsymbol{K}) \cdot t). \tag{2.19}$$

The prefactors, $w_p(\Delta \boldsymbol{K})$, are given by

$$w_p(\Delta \boldsymbol{K}) = \left| \sum_{i} \sqrt{c_i} b_i^p \right|^2, \tag{2.20}$$

where c_i is the concentration of adsorbates on sites of lattice i and b_i^p the pth eigenvector of matrix $\boldsymbol{B}$. In contrast to the simple model by Chudley and Elliot, the ISF for hopping on a non-Bravais lattice is a sum of m exponential functions, where m is determined by the number of sub-lattices, with the weights w_p describing the

contribution of each exponential to the ISF. Typically, some exponential functions have zero intensity ($w_p = 0$), so that the number of decays is $\leq m$. In Chaps. 5 and 6, hopping on hollow and/or bridge sites on a Cu(111) surface is discussed. Therefore, the models for these particular non-Bravais lattices are summarised below.

2.4.1.1 Jump Diffusion on Threefold Hollow Sites

In the case of hollow sites, hcp and fcc sites form two separate sub-lattices, thus m equals 2. The analytical solution for this model, as derived in [33], is as follows:

$$
\begin{aligned}
I(\Delta\boldsymbol{K},t)_{<1\bar{1}0>} &= \frac{c_1}{n_1}\left|1-\lambda\frac{4\cos\left(\frac{\Delta\boldsymbol{K}a}{2}\right)+2}{3\lambda-3+z}\right|^2 \exp\left(-\frac{\nu_{12}}{6\lambda}(3\lambda+3+z)t\right) \\
&\quad + \frac{c_1}{n_2}\left|1-\lambda\frac{4\cos\left(\frac{\Delta\boldsymbol{K}a}{2}\right)+2}{3\lambda-3-z}\right|^2 \exp\left(-\frac{\nu_{12}}{6\lambda}(3\lambda+3-z)t\right) \\
n_{1,2} &= 1+\lambda\left(\frac{4\cos\left(\frac{\Delta\boldsymbol{K}a}{2}\right)+2}{3\lambda-3\pm z}\right)^2 \\
z &= \sqrt{9\lambda^2+16\lambda\cos^2\left(\frac{\Delta\boldsymbol{K}a}{2}\right)+16\lambda\cos\left(\frac{\Delta\boldsymbol{K}a}{2}\right)-14\lambda+9} \\
I(\Delta\boldsymbol{K},t)_{<11\bar{2}>} &= \frac{c_1}{m_1}\left|1-2\lambda\frac{\exp\left(i\frac{\Delta\boldsymbol{K}a}{\sqrt{3}}\right)+2\exp\left(-i\frac{\Delta\boldsymbol{K}a}{2\sqrt{3}}\right)}{3(\lambda-1+y)}\right|^2 \exp\left(-\frac{\nu_{12}}{2\lambda}(\lambda+1+y)t\right) \\
&\quad + \frac{c_1}{m_2}\left|1-2\lambda\frac{\exp\left(i\frac{\Delta\boldsymbol{K}a}{\sqrt{3}}\right)+2\exp\left(-i\frac{\Delta\boldsymbol{K}a}{2\sqrt{3}}\right)}{3(\lambda-1-y)}\right|^2 \exp\left(-\frac{\nu_{12}}{2\lambda}(\lambda+1-y)t\right) \\
m_{1,2} &= 1+4\lambda\left|\frac{\exp\left(i\frac{\Delta\boldsymbol{K}a}{\sqrt{3}}\right)+2\exp\left(-i\frac{\Delta\boldsymbol{K}a}{2\sqrt{3}}\right)}{3(\lambda-1\pm y)}\right|^2 \\
y &= \sqrt{\lambda^2+\frac{2\lambda}{9}\left(8\cos\left(\frac{\sqrt{3}\Delta\boldsymbol{K}a}{2}\right)+1\right)+1}
\end{aligned}
\tag{2.21}
$$

The precise form of these equations is of little importance at this point, but it should be noted that the ISFs for both azimuths consist of a sum of two exponential functions. The lattice constant a—which is 2.55 Å for Cu(111) [34]—defines the periodicity of the prefactors and exponentials with $\Delta\boldsymbol{K}$, while the absolute height of the curves is given by the jump frequency, ν_{12}. The parameter λ, which is the ratio between the jump rates from fcc to hcp and from hcp to fcc sites, determines the relative ratios of prefactors and exponentials, and is given by the adsorption energy difference, ΔE, of the sites through

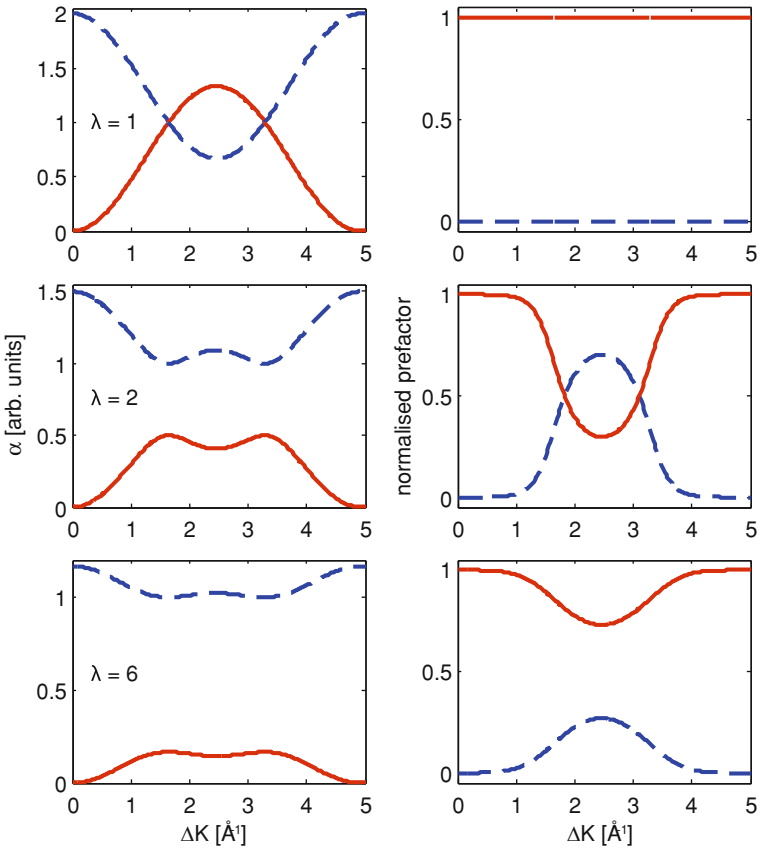

Fig. 2.10 Illustration of the jump diffusion model for hopping on fcc and hcp hollow sites on Cu(111), projected onto the $\langle 1\bar{1}0 \rangle$ azimuth. The $\Delta \boldsymbol{K}$ dependence of the two exponentials (*left column*) and corresponding normalised prefactors (*right column*) are presented for degenerate sites ($\lambda = 1$) in the top panels, and for increasingly non-degenerate sites beneath ($\lambda = 2$ and $\lambda = 6$)

$$\lambda = \exp\left(\frac{\Delta E}{k_B T}\right), \tag{2.22}$$

where k_B is the Boltzmann constant and T the temperature. $\Delta E = 0$ implies λ equal to 1, while $\lambda > 1$ for energetically different sites.

As is apparent in Fig. 2.8, the jump vectors from fcc and hcp sites give the same projection along the $\langle 1\bar{1}0 \rangle$ azimuth, yet different projections in the $\langle 11\bar{2} \rangle$ direction. The ISF therefore exhibits a single exponential function in the $\langle 1\bar{1}0 \rangle$ azimuth when both hollow sites are equivalent, as illustrated in the top panels of Fig. 2.10 where the intensity of the fast decay is zero for all momentum transfer values. For energetically different sites, the second decay gains in intensity, as apparent in the lower panels where results for increasing λ are shown. Along the $\langle 11\bar{2} \rangle$ azimuth, a sum of

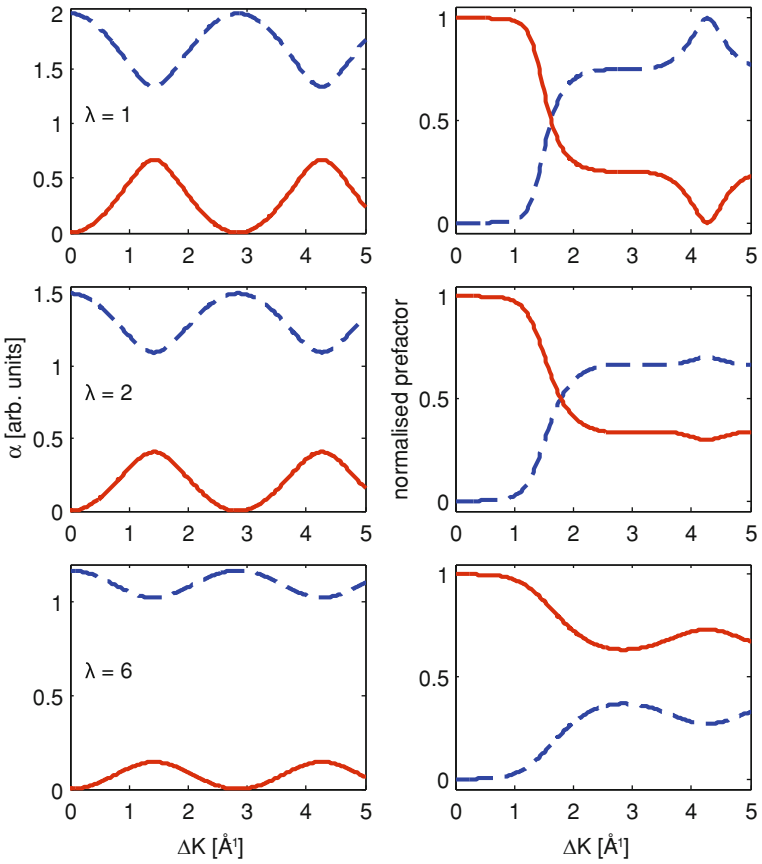

Fig. 2.11 Illustration of the jump diffusion model for hopping on fcc and hcp hollow sites on Cu(111), projected onto the $\langle 11\bar{2} \rangle$ azimuth. The $\Delta \boldsymbol{K}$ dependence of the two exponentials (*left column*) and corresponding normalised prefactors (*right column*) are presented for degenerate sites ($\lambda = 1$) in the top panels, and for increasingly non-degenerate sites beneath ($\lambda = 2$ and $\lambda = 6$)

two exponentials is observed at certain $\Delta \boldsymbol{K}$ positions for all values of λ, as shown in Fig. 2.11.

2.4.1.2 Jump Diffusion on Twofold Bridge Sites

Jump diffusion on a lattice of twofold bridge sites on a Cu(111) substrate is conceptually simpler since all bridge sites are always energetically equal. The analytical solution therefore does not include a parameter λ and the relative ratios of the exponentials and prefactors are constant:

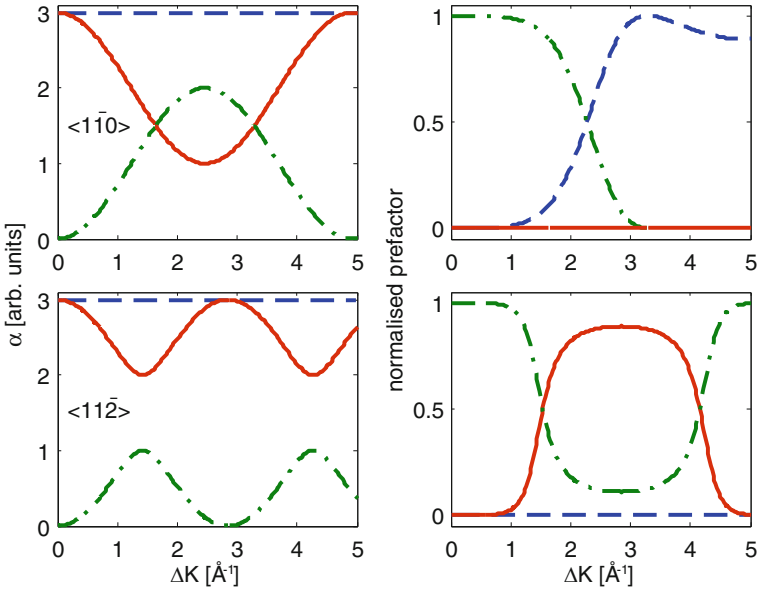

Fig. 2.12 Illustration of the jump diffusion model for hopping on bridge sites on Cu(111), projected onto the $\langle 1\bar{1}0\rangle$ (*top row*) and $\langle 11\bar{2}\rangle$ azimuths (*bottom row*). The $\Delta\boldsymbol{K}$ dependence of the three exponentials (*left column*) and corresponding normalised prefactors (*right column*) are presented

$$
\begin{aligned}
I(\Delta\boldsymbol{K},t)_{\langle 1\bar{1}0\rangle} &= c_1 \frac{\left(2\cos\left(\frac{\Delta\boldsymbol{K}a}{4}\right)-2\right)^2}{4\cos^2\left(\frac{\Delta\boldsymbol{K}a}{4}\right)+2}\exp(-3\nu_{12}t) \\
&\quad + c_1 \frac{\left(2\cos\left(\frac{\Delta\boldsymbol{K}a}{4}\right)+1\right)^2}{2\cos^2\left(\frac{\Delta\boldsymbol{K}a}{4}\right)+1}\exp\left(-\nu_{12}\left(1-\cos\left(\frac{\Delta\boldsymbol{K}a}{2}\right)\right)t\right) \\
I(\Delta\boldsymbol{K},t)_{\langle 11\bar{2}\rangle} &= \frac{c_1}{y^2+y}\left(2\cos\left(\frac{\Delta\boldsymbol{K}a\sqrt{3}}{4}\right)+1+y\right)^2\exp\left(-\frac{(3-y)\nu_{12}}{2}t\right) \\
&\quad + \frac{c_1}{y^2-y}\left(2\cos\left(\frac{\Delta\boldsymbol{K}a\sqrt{3}}{4}\right)+1-y\right)^2\exp\left(-\frac{(3+y)\nu_{12}}{2}t\right) \\
y &= \sqrt{8\cos^2\left(\frac{\Delta\boldsymbol{K}a\sqrt{3}}{4}\right)+1}
\end{aligned}
\tag{2.23}
$$

While there are three symmetrically different bridge sites (cf. Fig. 2.8), i.e. $m = 3$, they only give two different projections in both crystal directions and one of the exponentials along both azimuths has zero intensity. The resulting exponentials and normalised prefactors are presented in Fig. 2.12.

2.4.1.3 Jump Diffusion on Hollow and Bridge Sites

In Chap. 6, a third case of hopping on a non-Bravais lattice is discussed, namely hopping from bridge to hollow site and vice versa. A total of five different sites and three different energy levels thus needs to be considered, expressed as a (5×5) $\boldsymbol{B}$ matrix. Due to the complexity of the problem, the ISF was not calculated analytically but instead a numerical solution was determined by defining $\boldsymbol{A}$, performing the similarity transform to obtain $\boldsymbol{B}$ and subsequently calculating the eigenvalues and eigenvectors of $\boldsymbol{B}$.

Two λ parameters define the level of degeneracy between the different sites, λ_1 for the relative energy of bridge sites and one type of hollow sites, and λ_2 for bridge sites and the other type of hollow sites. In the case of degeneracy between fcc and hcp sites ($\lambda_1 = \lambda_2$), all intensity goes into three exponentials along $\langle 1\bar{1}0 \rangle$ and four along $\langle 11\bar{2} \rangle$, as shown in Figs. 2.13 and 2.14, respectively. Keeping the hollow sites degenerate but varying the energy difference between hollow and bridge sites, the ratio of the exponentials (left column in the Figures) changes, opening a gap when approaching either extreme of adsorption on hollow sites ($\lambda \to \infty$) or bridge sites alone ($\lambda \to 0$). When $\lambda_1 = \lambda_2 = 1.5$, bridge and hollow sites are weighted equally, as there are three bridge but only two hollow sites in a unit cell, and maximum symmetry of the exponentials is reached (cf. centre panels in Figs. 2.13 and 2.14).

When neither λ parameters equal 1, all five components contribute to the total intensity, yielding a sum of five exponentials in the ISF. Varying either one or both λ parameters, changes the ratio of the different exponentials, generating large gaps when a high level of degeneracy is obtained (cf. Figs. 2.15 and 2.16).

Finally, it should be noted that a single exponential decay is observed at approximately $\Delta\boldsymbol{K} < 0.7$ Å for all of these jump diffusion models. Experiments where a simple lineshape is desired to facilitate interpretation of the data, such as, for example, in the investigation of the temperature dependence of the dephasing rate at fixed momentum transfer, should therefore be performed in this regime (cf. Sect. 5.4.3).

2.4.2 Lateral Interactions: De Gennes Narrowing

Repulsive lateral interactions amongst adsorbates lead to a deviation from the $\alpha(\Delta\boldsymbol{K})$ curves predicted by analytical models described in the previous section, as first reported by de Gennes in 1959 [35]. Adsorbates repelling each other prefer a long-range quasi-hexagonal structure. The result is a preferred average distance between the adsorbates—dependent on the coverage—and reduced mobility on these length scales. When adsorbates approach each other, on the other hand, their mobility increases compared to that of non-repelling species. This effect creates a dip feature, termed "de Gennes narrowing", and a peak at lower $\Delta\boldsymbol{K}$ overlayed over the standard $\alpha(\Delta\boldsymbol{K})$ curves, as illustrated in Fig. 2.17. The dashed line shows the result from a molecular dynamics (MD) simulation for a single adsorbate particle, hence

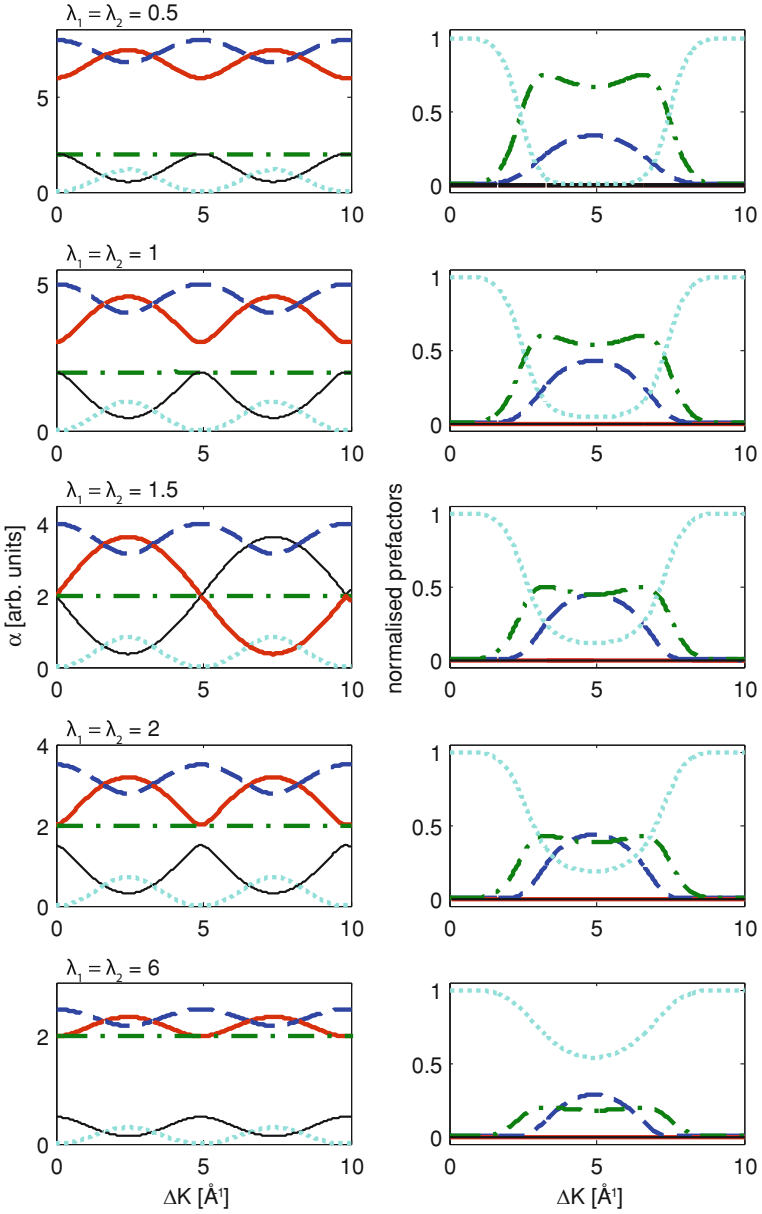

Fig. 2.13 Illustration of the jump diffusion model for hopping on bridge and degenerate fcc and hcp hollow sites on Cu(111), projected onto the $\langle 1\bar{1}0 \rangle$ azimuth. The $\Delta \boldsymbol{K}$ dependence of the exponentials (*left column*) and corresponding normalised prefactors (*right column*) are presented for varying levels of degeneracy between bridge and hollow sites. $\lambda_1 = \lambda_2 = 1$ is the case of degenerate bridge, fcc and hcp sites

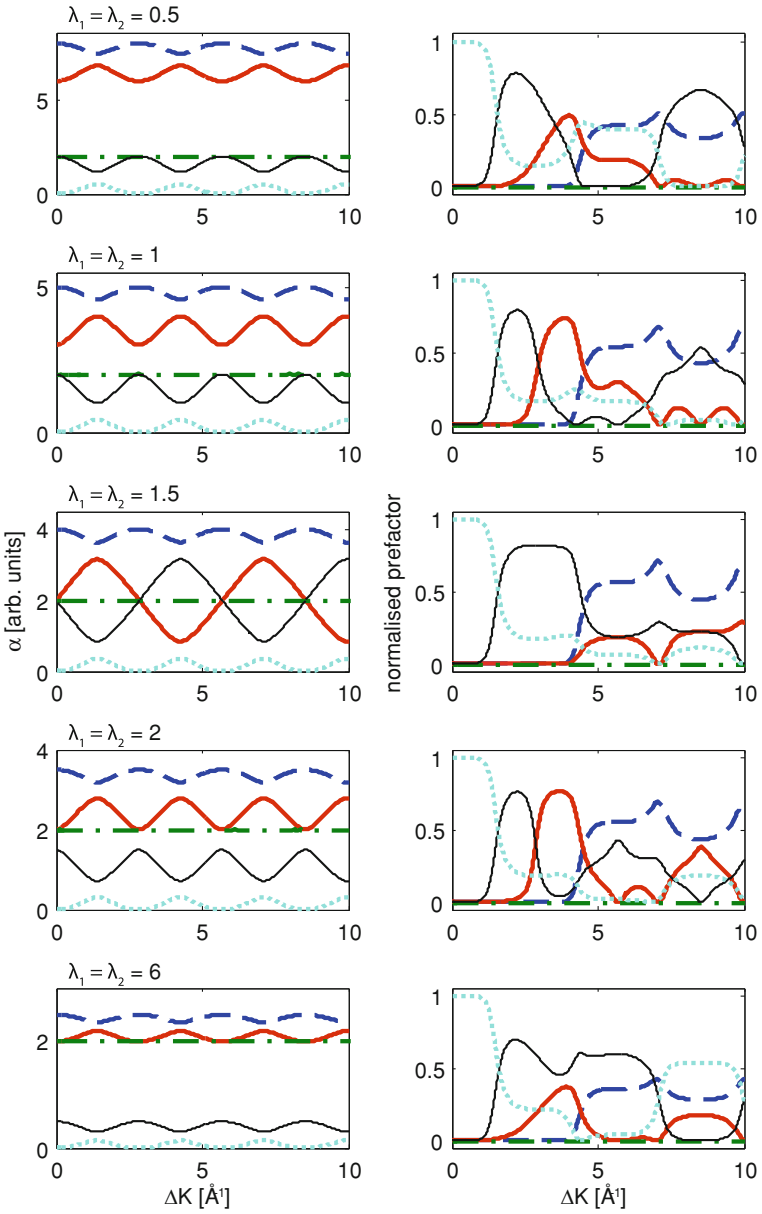

Fig. 2.14 Illustration of the jump diffusion model for hopping on bridge and degenerate fcc and hcp hollow sites on Cu(111), projected onto the $\langle 11\bar{2} \rangle$ azimuth. The $\Delta \boldsymbol{K}$ dependence of the exponentials (*left column*) and corresponding normalised prefactors (*right column*) are presented for varying levels of degeneracy between bridge and hollow sites. $\lambda_1 = \lambda_2 = 1$ is the case of degenerate bridge, fcc and hcp sites

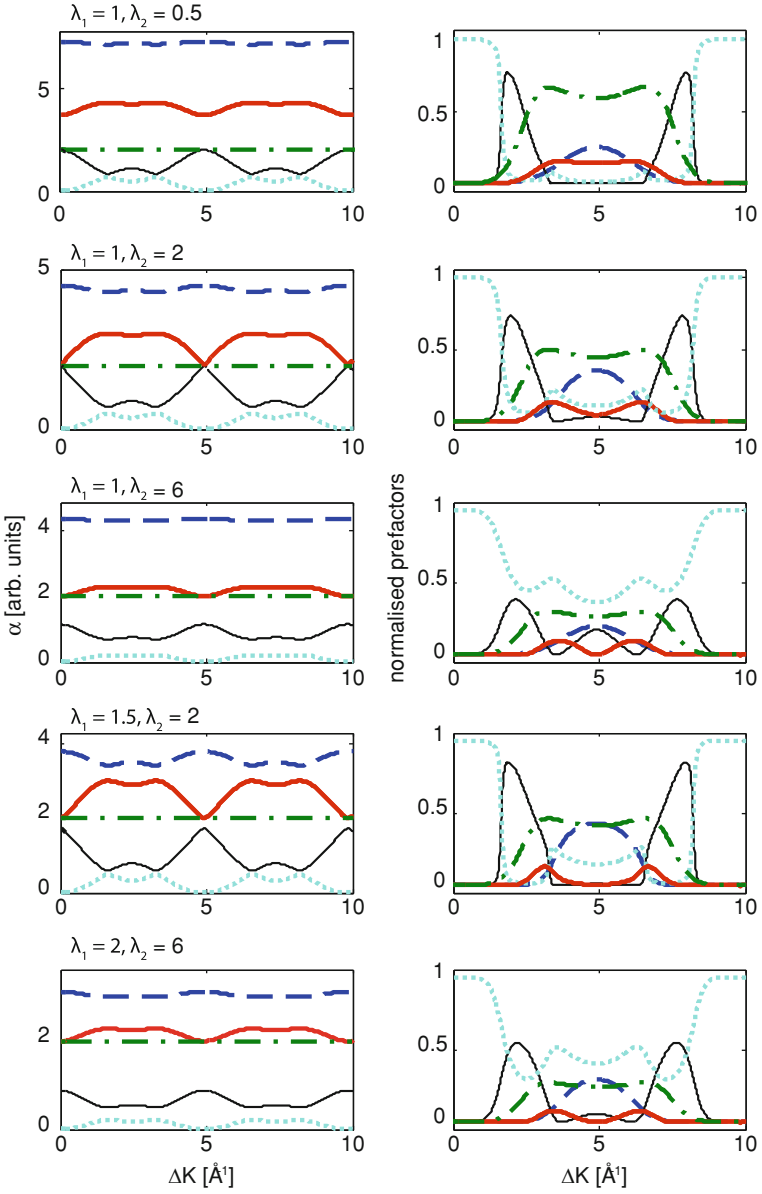

Fig. 2.15 Illustration of the jump diffusion model for hopping on bridge, fcc and hcp sites on Cu(111), projected onto the $\langle 1\bar{1}0 \rangle$ azimuth. The $\Delta \boldsymbol{K}$ dependence of the exponentials (*left column*) and corresponding normalised prefactors (*right column*) are presented for varying levels of degeneracy between bridge, fcc and hcp sites, where λ_1 defines the level of degeneracy between bridge and one type of hollow sites, while λ_2 relates bridge and the other type of hollow site

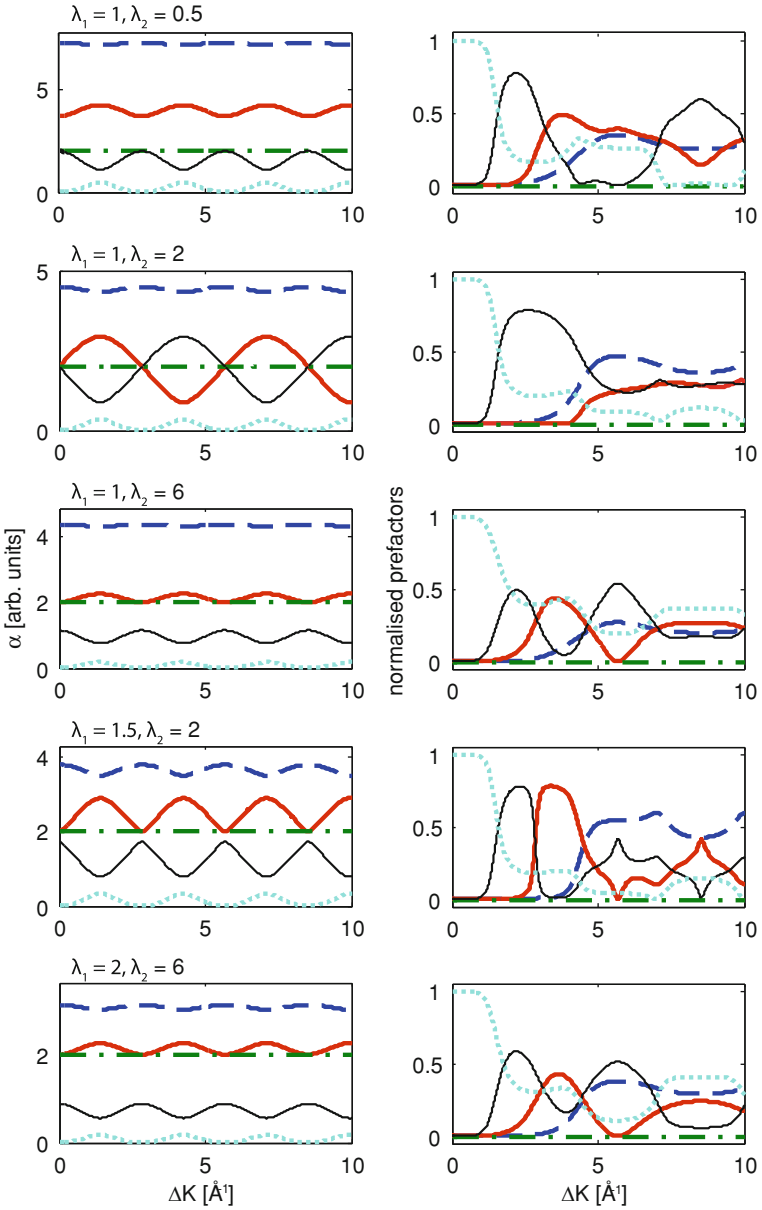

Fig. 2.16 Illustration of the jump diffusion model for hopping on bridge, fcc and hcp sites on Cu(111), projected onto the $\langle 11\bar{2} \rangle$ azimuth. The $\Delta \boldsymbol{K}$ dependence of the exponentials (*left column*) and corresponding normalised prefactors (*right column*) are presented for varying levels of degeneracy between bridge, fcc and hcp sites, where λ_1 defines the level of degeneracy between bridge and one type of hollow sites, while λ_2 relates bridge and the other type of hollow site

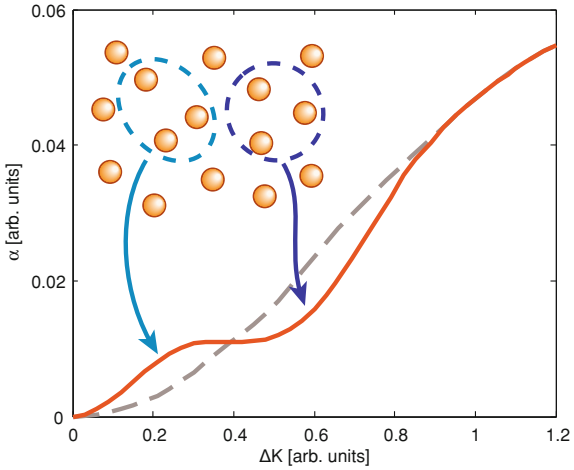

Fig. 2.17 Schematic illustration of the effect lateral interactions have on the $\alpha(\Delta \boldsymbol{K})$ curve in a HeSE experiment. A single particle MD simulation, presented as a *dashed line*, produces a sinusoidal curve, while an identical simulation of 40 interacting adsorbates, shown as a *solid line*, exhibits a de Gennes peak and dip feature. The peak can be explained by increased mobility of adsorbates at certain length scales due to strong repulsion, while the dip (de Gennes narrowing) is evidence for decreased mobility where a quasi-hexagonal arrangement is found

it includes no repulsive interactions and a smooth sinusoidal curve is observed. The solid line presents an equivalent simulation for 40 interacting adsorbates. A peak appears at low $\Delta \boldsymbol{K}$ values, illustrating increased mobility of certain length scales, while a dip occurs at the length scale of the quasi-hexagonal arrangement.

The position of the dip can be used to estimate the coverage,

$$\Theta = \frac{a^2}{r^2}, \tag{2.24}$$

from the average nearest-neighbour distance, r, and the substrate lattice constant, a [23]. By approximating the local order as a hexagonal lattice [23], the nearest-neighbour distance can be deduced from the momentum transfer position of the de Gennes dip, ΔK_{dip}, as

$$r = \frac{4\pi}{\sqrt{3} \cdot \Delta \boldsymbol{K}_{dip}}. \tag{2.25}$$

2.4.3 Molecular Dynamics Simulations

In addition to interpreting experimental data using analytical models for diffusion, MD simulations can be performed which give a more complete picture of the motion,

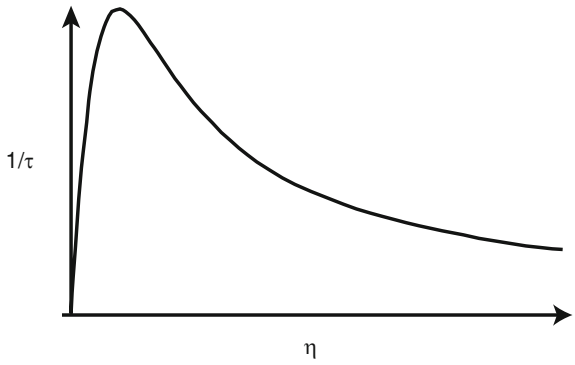

Fig. 2.18 Jump frequency as a function of friction, illustrating the "turnover" from low to high friction (adapted from [40])

providing information about the nature of lateral interactions and the friction as well as the type of diffusion [36–38]. In a classical simulation, the diffusion of an adsorbate particle is described using the 2D Langevin equation

$$m\ddot{\boldsymbol{R}}_i = -\nabla V(\boldsymbol{R}_i) - m\eta\dot{\boldsymbol{R}}_i + \xi(t) + \sum_{i \neq j} F_{i,j}, \tag{2.26}$$

where the trajectories for the i-th adsorbate particle with velocity $\dot{\boldsymbol{R}}_i$ are calculated for motion on a potential energy surface (PES), $V(\boldsymbol{R}_i)$. The friction coefficient, η, describes the energy exchange between adsorbate and substrate and a random impulse term, ξ, ensures that the total energy of the system remains preserved. For simulations of multiple adsorbate particles, $F_{i,j}$ models the pairwise lateral interactions between particle i and particle j, for example by dipole–dipole interactions. The input parameters $V(\boldsymbol{R}_i)$, η and $F_{i,j}$ are varied iteratively to obtain a realistic description of the experimental data.

In addition to interpreting experimental data, MD simulations can be used to study the effect of individual parameters on the adsorbate system, which is often not possible in an experiment. Varying the friction coefficient while keeping all other parameters constant, for example, provides information about the rate of energy exchange between adsorbate and substrate. Transition state theory (TST) is widely used to describe diffusion through the population of the transition state, determining the rate of diffusion. TST assumes that every atom in a transition state originates from an adjacent adsorption well, which is only true in certain cases. In most real systems, a deviation from TST is observed, as first discussed by Kramers in 1940 [39]. The jump frequency, $\nu = 1/\tau$, as a function of η is shown in Fig. 2.18 [40]. A corresponding curve obtained by MD simulations for Cp/Cu(111) is presented in Chap. 5. In the case of low friction, the rate of energy exchange between adsorbate and substrate is small and once the diffusing species has acquired enough energy to overcome the barrier, it "rollercoasters" over many barriers. This implies that only a fraction of the species in the transition state comes from the adjacent well and thus the actual jump frequency is lower than predicted by TST. In the case of high friction, the

diffusing particle changes its energy, and hence its velocity, so frequently that it does not move by a direct route between adsorption sites but rather moves by a random walk leading to re-crossings of the transition state. Since the same atom can be in the transition state a number of times, assuming that each atom in the transition state has just come from the adjacent adsorption site yet again overestimates the jump rate. TST therefore only gives a realistic description for systems at the "turnover" point between low and high friction, i.e. on the peak of the curve.

References

1. A.P. Jardine, S. Dworski, P. Fouquet, G. Alexandrowicz, D.J. Riley, G.Y.H. Lee, J. Ellis, W. Allison, Ultrahigh-resolution spin-echo measurements of surface potential energy landscapes. Science **304**, 1790 (2004)
2. A.P. Jardine, H. Hedgeland, G. Alexandrowicz, W. Allison, J. Ellis, Helium-3 spin-echo: principles and application to dynamics at surfaces. Prog. Surf. Sci. **84**, 323 (2009)
3. A.P. Jardine, J. Ellis, W. Allison, Quasi-elastic helium-atom scattering from surfaces: experiment and interpretation. J. Phys. Condens. Matter **14**, 6173–6191 (2002)
4. A.P. Jardine, G. Alexandrowicz, H. Hedgeland, W. Allison, J. Ellis, Studying the microscopic nature of diffusion with helium-3 spin-echo. Phys. Chem. Chem. Phys. **11**, 3355 (2009)
5. D. Farías, K.-H. Rieder, Atomic beam diffraction from solid surfaces. Rep. Prog. Phys. **61**, 1575–1664 (1998)
6. A.P. Graham, The low energy dynamics of adsorbates on metal surfaces investigated with helium atom scattering. Surf. Sci. Rep. **49**, 115–168 (2003)
7. G. Alexandrowicz, A.P. Jardine, Helium spin-echo spectroscopy: studying surface dynamics with ultra-high-energy resolution. J. Phys. Condens. Matter **19**, 305001 (2007)
8. M.J. Bée, *Quasielastic Neutron Scattering* (Hilger, Bristol, 1988)
9. L. Van Hove, Correlations in space and time and born approximation scattering in systems of interacting particles. Phys. Rev. **95**(1), 249–262 (1954)
10. G. Vineyard, Scattering of slow neutrons by a liquid. Phys. Rev. **110**(5), 999–1010 (1958)
11. J.W.M. Frenken, B.J. Hinch, J.P. Toennies, He scattering study of diffusion at a melting surface. Surf. Sci. **211/212**, 21–30 (1989)
12. M. DeKieviet, D. Dubbers, C. Schmidt, D. Scholz, U. Spinola, ^{3}He spin echo: new atomic beam technique for probing phenomena in the neV range. Phys. Rev. Lett. **75**, 1919–1922 (1995)
13. M. DeKieviet, D. Dubbers, M. Klein, C. Schmidt, M. Skrzipczyk, Surface science using molecular beam spin echo. Surf. Sci. **377–379**, 112–117 (1997)
14. F. Mezei, Neutron spin echo: a new concept in polarized thermal neutron techniques. Z. Physik **255**, 146 (1972)
15. P. Fouquet, A.P. Jardine, S. Dworski, G. Alexandrowicz, W. Allison, J. Ellis, Thermal energy ^{3}He spin-echo spectrometer for ultrahigh resolution surface dynamics measurements. Rev. Sci. Instrum. **76**, 53109 (2005)
16. H. Hedgeland, A.P. Jardine, W. Allison, J. Ellis, Anomalous attenuation at low temperatures in a high intensity helium beam source. Rev. Sci. Instrum. **76**, 123111 (2005)
17. H. Hedgeland, P.R. Kole, W. Allison, J. Ellis, A.P. Jardine, An improved high intensity recycling helium-3 beam source. Rev. Sci. Instrum. **80**, 76110 (2009)
18. A.P. Jardine, P. Fouquet, J. Ellis, W. Allison, Hexapole magnet system for thermal energy ^{3}He atom manipulation. Rev. Sci. Instrum. **72**(10), 3834–3841 (2001)
19. P.R. Kole, Dynamics and morphology of metal and metal oxide surfaces. Ph.D. thesis, University of Cambridge 2011
20. H. Hedgeland, The Development of Quasi-Elastic Helium-3 Spin-Echo Spectroscopy as a Tool for the Study of Surface Dynamics. Ph.D. thesis, University of Cambridge 2006

21. A.R. Alderwick, A.P. Jardine, H. Hedgeland, D.A. MacLaren, W. Allison, J. Ellis, Simulation and analysis of solenoidal ion sources. Rev. Sci. Instrum. **79**, 123301 (2008)
22. D.M. Chisnall, A high sensitivity detector for helium atom scattering. Ph.D. thesis, University of Cambridge 2012
23. A.P. Jardine, G. Alexandrowicz, H. Hedgeland, R.D. Diehl, W. Allison, J. Ellis, Vibration and diffusion of Cs atoms on Cu(001). J. Phys. Condens. Matter **19**, 305010 (2007)
24. D.J. Ward, A study of spin-echo lineshapes in helium atom scattering from adsorbates. Ph.D. thesis, University of Cambridge 2013
25. J.L. Vega, R. Guantes, S. Miret-Artés, D.A. Micha, Collisional line shapes for low frequency vibrations of adsorbates on a metal surface. J. Chem. Phys. **121**, 8580 (2004)
26. R. Martínez-Casado, J.L. Vega, A.S. Sanz, S. Miret-Artés, Line shape broadening in surface diffusion of interacting adsorbates with quasielastic He atom scattering. Phys. Rev. Lett. **98**, 216102 (2007)
27. E.M. McIntosh, P.R. Kole, M. El-Batanouny, D.M. Chisnall, J. Ellis, W. Allison, Measurement of the phason dispersion of misfit dislocations on the Au(111) surface. Phys. Rev. Lett. **110**, 086103 (2013)
28. R. Gomer, Diffusion of adsorbates on metal surfaces. Rep. Prog. Phys. **53**, 917–1002 (1990)
29. T. Ala-Nissila, R. Ferrando, S.C. Ying, Collective and single particle diffusion on surfaces. Adv. Phys. **51**(3), 949 (2002)
30. C.T. Chudley, R.J. Elliot, Neutron scattering from a liquid on a jump diffusion model. Proc. Phys. Soc. **77**(2), 353–361 (1960)
31. J.M. Rowe, K. Sköld, H.E. Flotow, J.J. Rush, Quasielastic neutron scattering by hydrogen in the α and β phases of vanadium hydride. J. Phys. Chem. Solids **32**, 41–54 (1971)
32. O.G. Randl, B. Sepiol, G. Vogl, R. Feldwisch, K. Schroeder, Quasielastic Mössbauer spectroscopy and quasielastic neutron scattering from non-Bravais lattices with differently occupied sublattices. Phys. Rev. B **49**, 8768 (1994)
33. F.E. Tuddenham, H. Hedgeland, A.P. Jardine, B.A.J. Lechner, B.J. Hinch, W. Allison, Lineshapes in quasi-elastic scattering from species hopping between non-equivalent surface sites. Surf. Sci. **604**, 1459–1475 (2010)
34. U. Harten, J.P. Toennies, C. Wöll, Helium time-of-flight spectroscopy of surface-phonon dispersion curves of the noble metals. Faraday Discuss. Chem. Soc. **80**, 137 (1985)
35. P.G. De Gennes, Liquid dynamics and inelastic scattering of neutrons. Physica **25**, 825–839 (1959)
36. J. Ellis, A.P. Graham, The use of quasielastic helium atom scattering to study correlated motion in adsorbate overlayers. Surf. Sci. **377**, 833 (1997)
37. G. Alexandrowicz, P.R. Kole, E.Y.M. Lee, H. Hedgeland, R. Ferrando, A.P. Jardine, W. Allison, J. Ellis, Observation of uncorrelated microscopic motion in a strongly interacting adsorbate system. J. Am. Chem. Soc. **130**, 6789–6794 (2008)
38. P.R. Kole, H. Hedgeland, A.P. Jardine, W. Allison, J. Ellis, G. Alexandrowicz, Probing the non-pairwise interactions between CO molecules moving on a Cu(111) surface. J. Phys. Condens. Matter **24**, 104016 (2012)
39. H.A. Kramers, Brownian motion in a field of force and the diffusion model of chemical reactions. Physica **7**(4), 284 (1940)
40. R. Zwanzig, *Nonequilibrium Statistical Mechanics* (Oxford University Press, Oxford, 2001)

http://www.springer.com/978-3-319-01179-0

Studying Complex Surface Dynamical Systems Using Helium-3 Spin-Echo Spectroscopy

Lechner, B.A.J.

2014, XV, 172 p. 98 illus., 39 illus. in color., Hardcover
ISBN: 978-3-319-01179-0